

Chapter 4

Decay and Phase Rotation Channel

4.1 Concept

The function of the phase rotation section of the Neutrino Factory is to reduce the energy spread of the collected muon beam to a manageable level that will allow reasonable throughput to subsequent system components. We see in Fig. 4.1 the consequences of allowing the beam to drift without the application of properly phased acceleration. In Fig. 4.2 we see the longitudinal structure of the beam after the application of our proposed three-stage phase rotation system.

For a Neutrino Factory the requirements on the longitudinal phase space are quite different than those for a muon collider. Unlike the muon beam for a muon collider we can permit the captured muon beam to grow in its longitudinal dimensions and then put it through a buncher system that will permit the cooling section downstream to be operated with rf cavities having relatively high frequency.

If the process is done with a single drift and single induction linac, relativistic effects cause a distortion of the rotated bunch such that the initially high energy particles end up with a larger energy spread than the initially low energy ones. The use of at least two induction linacs, with a drift between them, allows this distortion to be greatly reduced.

It is natural for both these induction linacs to be bipolar, with initial deceleration and later acceleration. For technical reasons, such bipolar voltage pulses have been avoided in the baseline design. In the case of the first linac, a hydrogen absorber is placed immediately after it to reduce the beam energy, allowing the first linac to be unipolar. This absorber also reduces the emittance, and is thus referred to as a “minicooler.” The absorber is in two parts, with a field reversal between them to avoid the generation of angular momentum.

4.2. Drift Sections

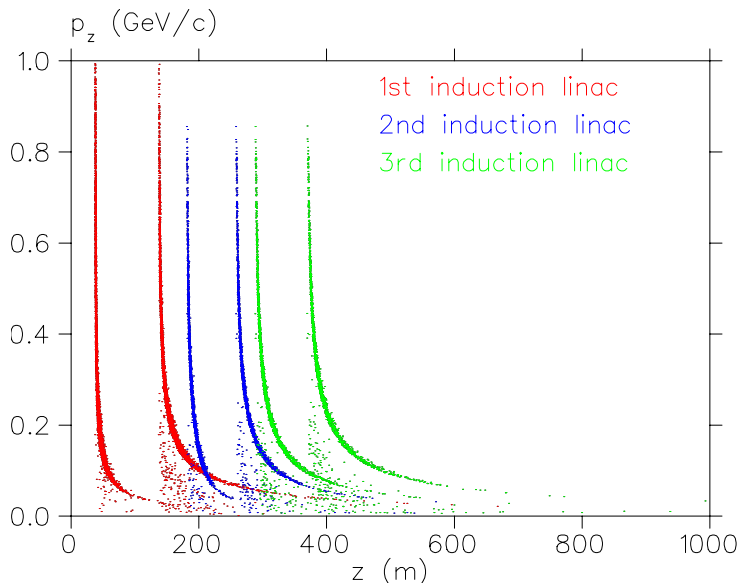


Figure 4.1: Beam longitudinal profile without phase rotation.

To avoid a bipolar second linac, it has been replaced with two linacs: the first unipolar decelerating, the second unipolar acceleration (A slightly less conventional bipolar second linac solution is discussed in Section [A.2.4](#)).

4.2 Drift Sections

A principal strategy for the drift sections of the capture/decay channel is to avoid the π -resonances that will be present due to the necessary periodic structure of the solenoidal magnetic field (resulting from gaps between the superconducting coils). Examples of these resonances are located at the minimum (odd- π) and maximum (even- π) points shown in Fig. [4.3](#). For drift sections, these $n\pi$ -resonance points are approximated by

$$p = \lambda \frac{Bc}{2\pi n} \quad (4.1)$$

where p is in units of eV/c, B is the average solenoidal field in Tesla, c is m/s and the period, λ , is in meters.

Particle losses in a 3 T periodic solenoidal system are confirmed in Fig. [4.4](#) where the spectrum of surviving particles after a 50 m drift is compared with the spectrum of the

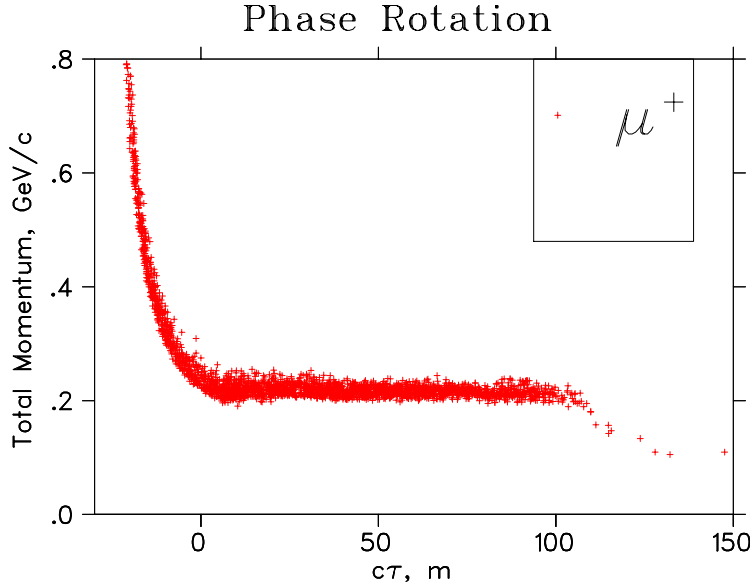


Figure 4.2: Beam longitudinal profile with non-distorting phase rotation.

source particles. The particle tracking for this example is done with ICOOL. Note the appearance of particle losses in the momentum band of 150–200 MeV/ c which agrees well with the predictions seen in Fig. 4.3. Hence, if we wish to avoid particle losses in the momentum region of 100 to 300 MeV/ c then a channel based on a 1.5 T solenoidal field and a 1 m period should be suitable.

We choose as the baseline for our decay channel the parameters $B = 1.25$ T and a period of 0.5 m. We extend this periodicity throughout the capture channel to include also the induction linac section, so that only the minicool section, with its single-flip solenoidal field does not exhibit this 0.5 m periodicity. Using ICOOL, we have compared the results of transporting the MARS-generated particles at the target through the exit of the third induction linac for both the case of 0.5 m periodicity and an artificial constant 1.25 T solenoidal field throughout the channel (excluding the minicool segment). We find that the total throughput of muons at the exit of the third induction linac is the same for both cases.

4.2. Drift Sections

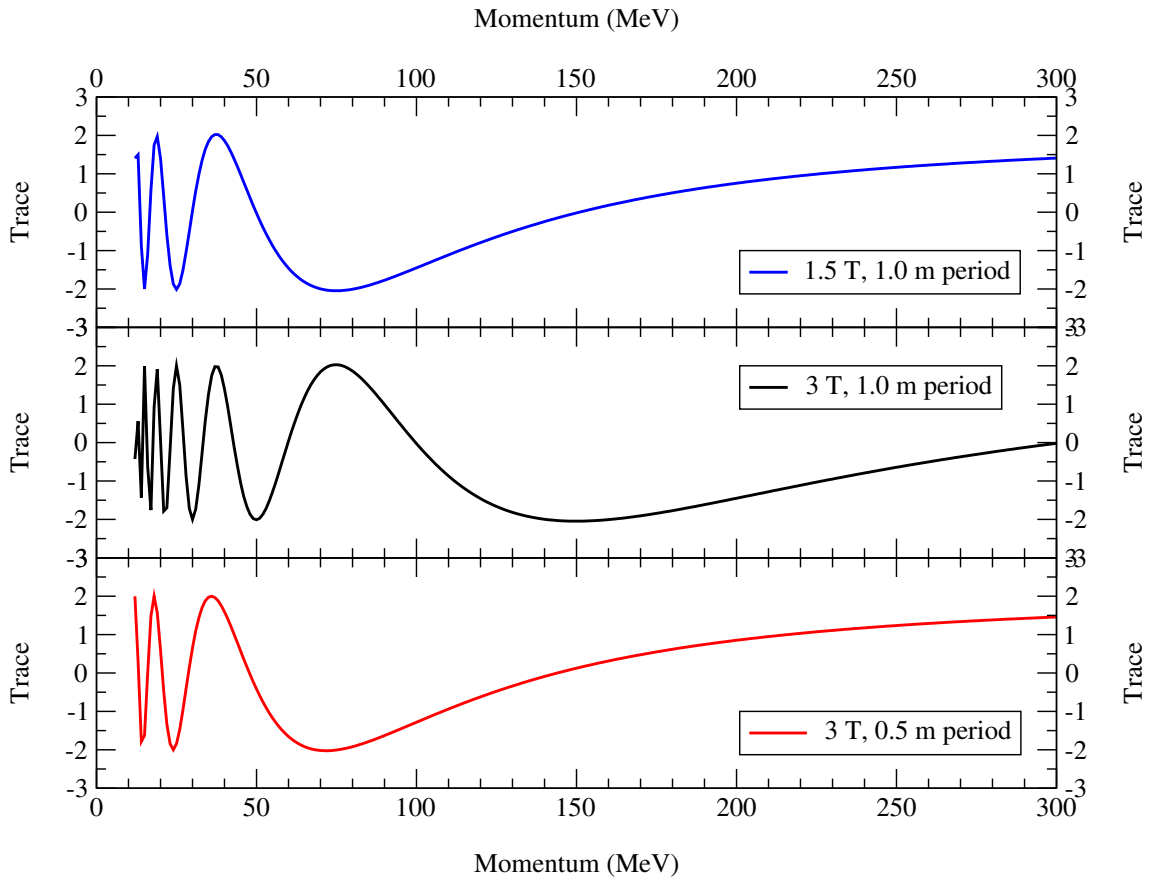


Figure 4.3: Location of $n\pi$ -resonances in a periodic solenoidal field.

3T channel with single 14cm gap

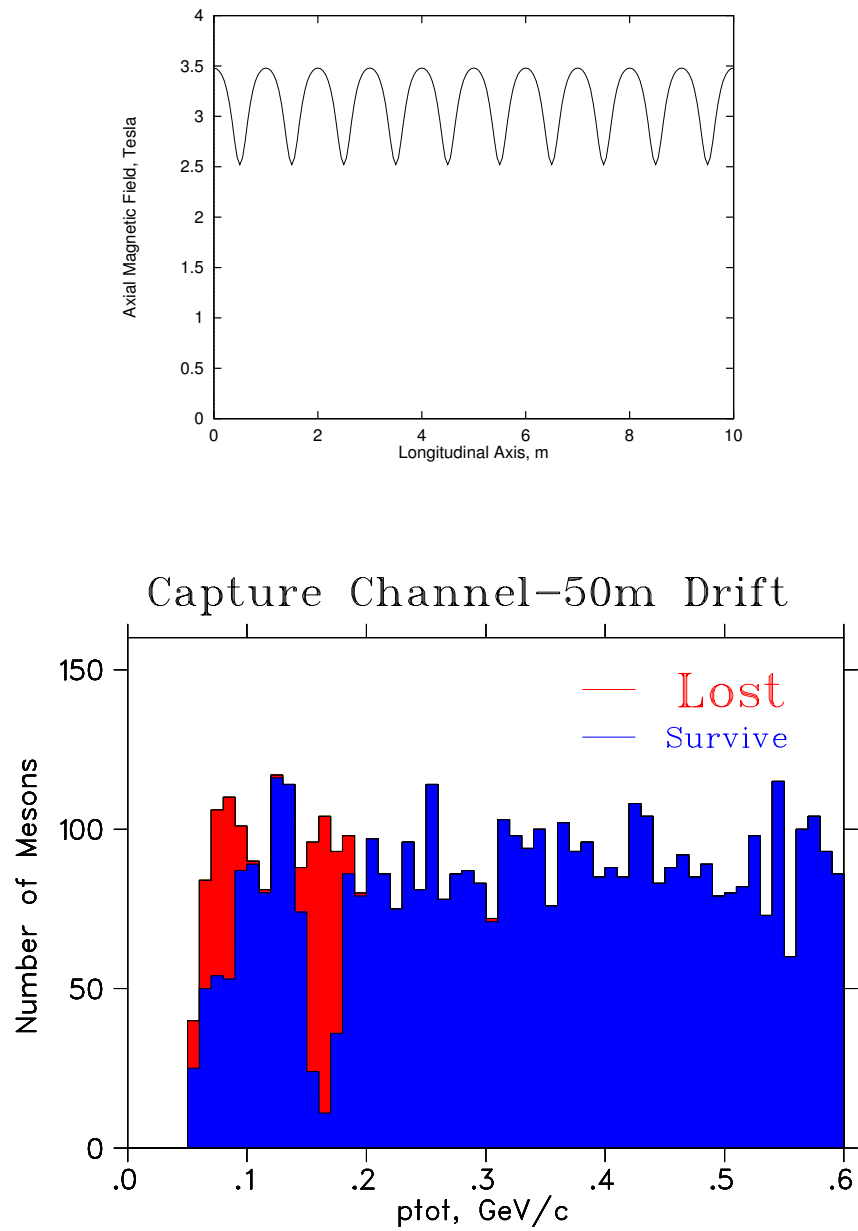


Figure 4.4: Particle losses after a 50 m drift in a 3 T, 1 m periodic solenoidal field

4.3 Induction Linacs

The muons drift first to spread out in time. The induction linacs then decelerate the early particles and accelerate the later ones. Three induction linacs are used with lengths of 100, 80 and 80 m, in a system that reduces distortion in the phase space of the rotated muon bunch and allows the induction linacs to operate with unipolar pulses. One additional feature of this design is that the 1.25 T transport solenoids are placed inside of the induction cores to avoid saturation of the ferrites. The induction linac units are similar to those being built for the DARHT project [1]; technical details are discussed in Chapter 9.

Figure 4.5 shows the pulse shapes of three induction linacs and Fig. 4.6 depicts a cross section of two units of the induction linac. The gaps in the solenoidal focusing, which lead to the periodicity described in Section 4.2, are apparent.

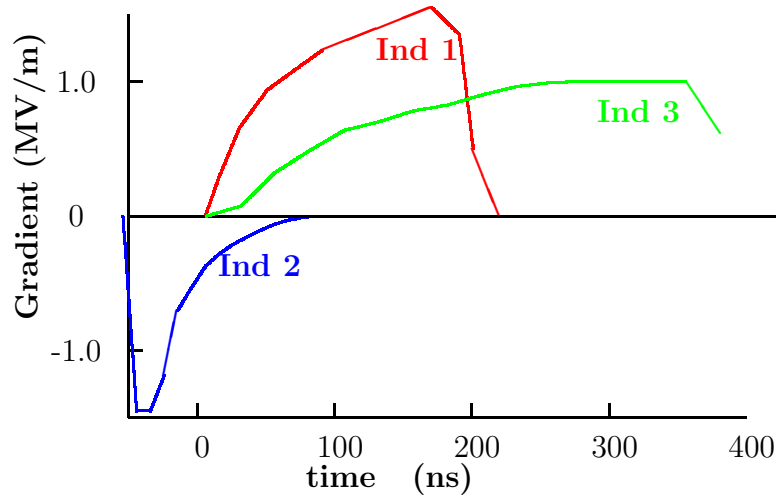


Figure 4.5: Pulse shapes of the three induction linacs.

4.4 The Solenoids

The decay and phase rotation region includes the IL1, the mini-cooler, IL2 and IL3, and extends from $z = 18$ m (from the target) to $z = 356$ m. Within this region, there are four types of solenoids.

4.4. The Solenoids

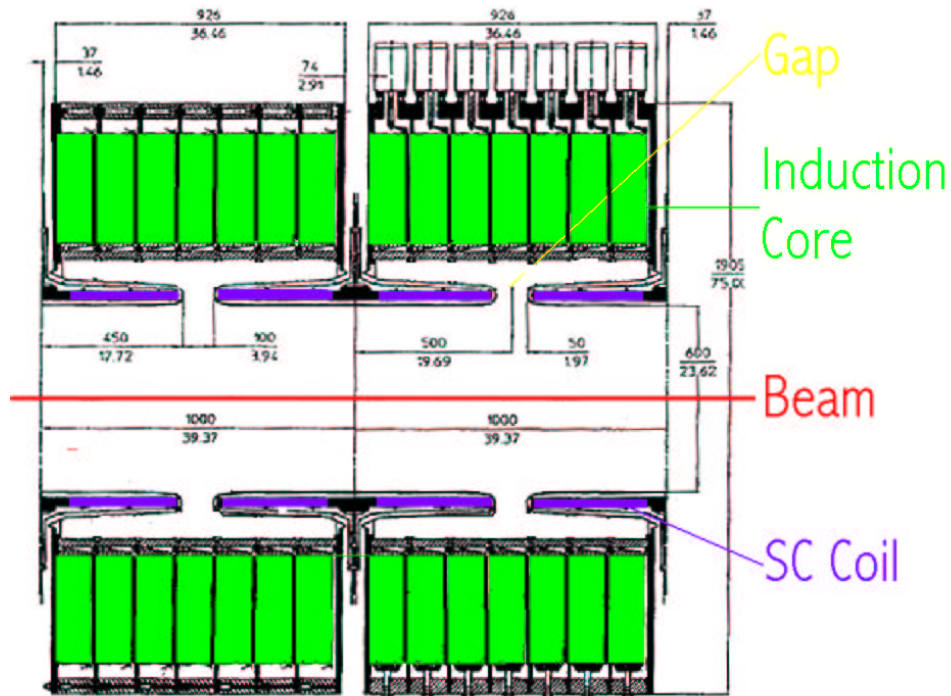


Figure 4.6: Cross section of two induction units.

1. From $z = 18$ m to $z = 36$ m, there is a decay section that has a warm bore diameter of 600 mm. Around this warm bore is a water-cooled copper shield that is 100 mm thick. The solenoid cryostat warm bore is thus 800 mm. The 18 m of decay solenoid is divided into six cryostats each 2.9 m long. This same type of magnet is used for the 9 m long mini-cooling sections on either side of the field-flip solenoid. As a result, there are twelve magnets of this type.
2. The IL1 solenoids, which extend from $z = 36$ m to $z = 146$ m, have a beam aperture of 600 mm diameter. Around the bore is a 10 mm thick water-cooled copper radiation shield. The warm bore of this magnet cryostat is thus 620 mm in diameter. There are 110 magnets of this type.
3. IL2 and IL3 and the drift between them extend, from $z = 166$ m to $z = 356$ m. These solenoids do not require a radiation shield and have a cryostat warm bore diameter of 600 mm. There are 190 magnets of this type.

4.5. Minicooling Absorbers

4. The field-flip solenoid between the two mini-cooling sections is 2 m long with a warm bore diameter of 400 mm. There is only one such magnet.

Table 4.1 shows the design parameters for the induction linac solenoids and the solenoids in the decay channel and mini-cooling channel. The 2-meter long field flip solenoid is not included in this table. Technical details of the magnets are discussed in Chapter 10.

4.5 Minicooling Absorbers

The baseline design includes two “minicooling” liquid-hydrogen absorbers, each 30 cm in radius and 1.75 m long, preceded by a thin beryllium sheet and separated by a field flip. ICOOL simulations have been used to propagate MARS-generated secondary particles from the primary target through the initial induction linac module to the minicool absorbers. Tables 4.2 and 4.3 give the estimated power deposition in these absorbers for each important particle species generated at the target. For each mode the total power deposited in the absorber is about 5 kW. As seen in Fig. 4.7, the power dissipation in the first absorber is peaked at the absorber’s upstream end. This energy dissipation peak is due to the arrival of low-energy protons which are generated at the target and conducted down the capture/decay channel. They are not removed by the induction linac because they are out of time with the higher velocity mesons and electrons. A beryllium sheet placed immediately before the liquid hydrogen absorber is used to absorb the low-energy protons and reduce the peak energy deposition in the first several cm of liquid hydrogen. However, even without this beryllium absorber foil, we find the volume power density in the liquid hydrogen to be manageable.

4.5.1 Handling the Average Heat Load

Even without detailed refrigeration studies, we can be confident about the overall power-handling capability of these absorbers based on experience with the Fermilab 15-foot bubble chamber. The 15-foot bubble chamber was cooled by a 6.7 kW refrigerator [2]. While considerably larger than a minicooling absorber, the bubble chamber had substantially lower beam-induced power dissipation; the large refrigeration plant was required to remove the heat generated by the work done on the fluid by the rapid-cycling expansion piston.

Each minicooling absorber will have refrigeration requirements comparable to that of the 15-foot bubble chamber. On the other hand, Table 4.4 shows that the refrigeration

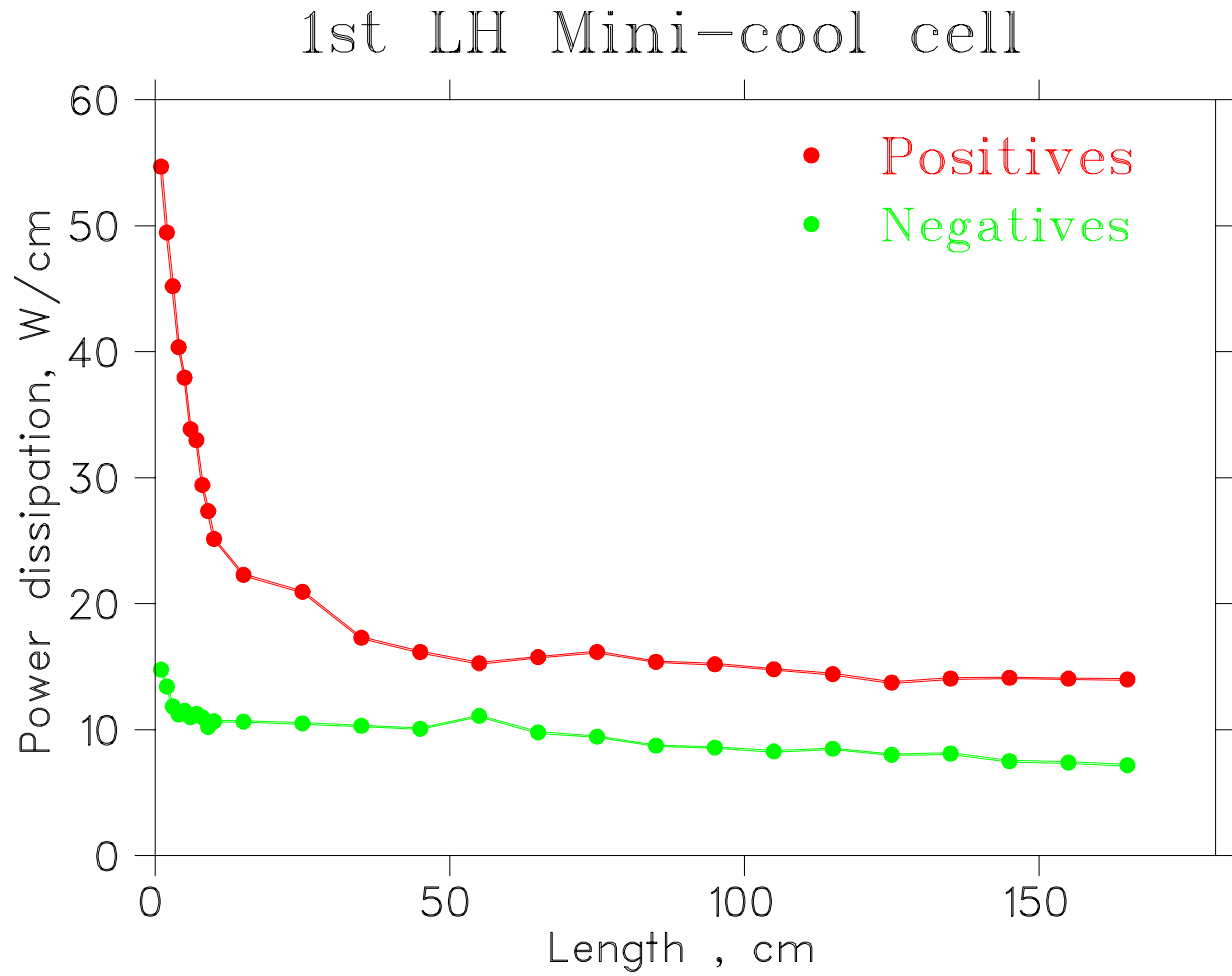


Figure 4.7: Power deposition along the length of the first minicool section.

4.5. Minicooling Absorbers

needed for the minicooling absorbers dominates that of the cooling channel itself (see Section 5.3.6) and the extra complexity and reliability impact of operating two 15-foot-bubble-chamber equivalents is worth avoiding if a practical alternative is available; these considerations motivate the minicooling alternatives considered in Section 14.4.

4.5.2 Handling the Peak Power Density

Figure 4.7 shows the power dissipation *vs.* position along the absorber, and Fig. 4.8 shows the transverse distribution. For comparison, the liquid-hydrogen target built for SLAC Experiment 158 [3] is designed to handle 700 W, uniformly distributed over 1.5 m of length but with about 1 mm rms transverse beam size. While the power per cm at the upstream end of the first minicooling absorber is more than 10 times that in SLAC E158, the power per cm³ is only about 10⁻³ of that in E158. We therefore conclude that the peak power density will not pose a problem and can be handled using one or the other of the approaches described elsewhere in this report (see Section 5.3.6).

4.5.3 Window Design

Unlike the case for the SFOFO absorbers, in the minicooling absorbers muon multiple scattering is dominated by the hydrogen, and muon-cooling performance hardly depends on the details of the window design. Furthermore, a hemispherical window shape, which minimizes the window thickness for a given strength, is practical for absorbers such as these, whose length far exceeds their diameter. The American Society of Mechanical Engineers (ASME) [4] specifies the minimum acceptable thickness for a hemispherical window as

$$t = \frac{0.5PR}{SE - 0.1P}, \quad (4.2)$$

where P is the differential pressure across the window, R the vessel radius, S the maximum allowable stress, and E the weld efficiency. For S , we follow ASME recommendations and use the smaller of 1/4 of the ultimate strength, S_u , or 2/3 of the yield strength, S_y ; in practice, for aluminum alloys, it is the ultimate strength that matters. If we machine the window with an integral flange out of a single disk of material, as for the cooling channel absorbers, there are no welds and we can take $E = 1$. For 1.2 atm operation, and given the ASME specification for 6061-T6 aluminum alloy, $S_u = 289$ MPa and we obtain $t = 250$ μ m. While a detailed finite-element analysis (taking into account the stresses imposed on the spherical shell by the stiff flange) may result in a somewhat thicker window, even windows as thick as 1 mm have been shown by simulation to have negligible effect on muon-cooling performance.

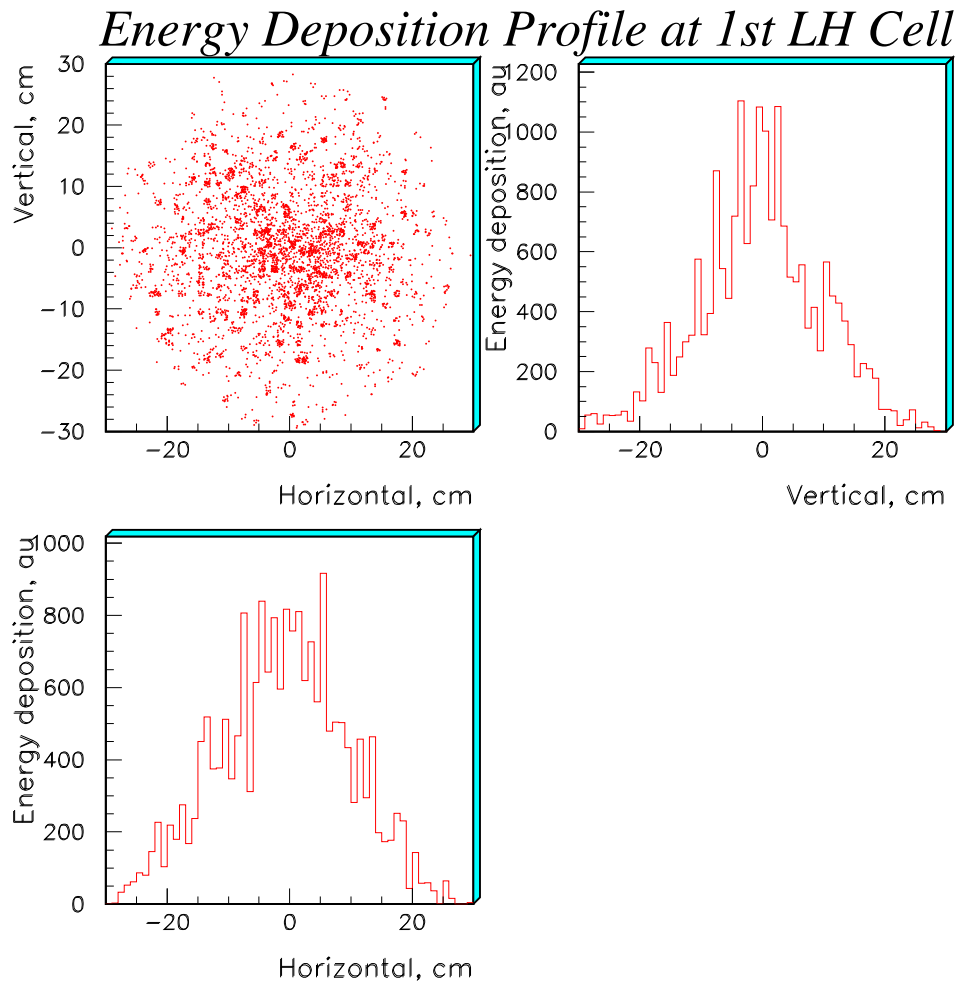


Figure 4.8: Transverse power deposition in the first minicool section.

4.6. Summary

4.6 Summary

The guiding principle of the design for the Capture/phase rotation section of the front end for the neutrino factory has been to achieve good performance while utilizing components based on at-hand technology. Key components include large aperture superconducting solenoids, 260 m of induction linac, and 3.5 m of liquid hydrogen absorbers. The gradients required for the induction linacs are between 1.55 and 1.0 MV/m. The muon beam delivered to the buncher has an rms energy spread, $\frac{\delta E}{E}$ of 4.4% and contains 0.49 μ /p within the $\pm 3.5\sigma$ boundaries of this energy spread.

Table 4.1: Decay, phase rotation, and minicool solenoid parameters.

| | IL1 Magnets | IL2,IL3 Magnets | Decay Channel Magnets |
|---|-----------------------|-----------------------|--------------------------|
| Magnet Mechanical Parameters | | | |
| No. of cells of this Type | 110 | 190 | 12 |
| Cell length (mm) | 1000.0 | 1000.0 | 3000.0 |
| Magnet cryostat length (mm) | 900.0 | 900.0 | 2900.0 |
| Magnet coil package length (mm) | 860.0 | 860.0 | 860.0 |
| Number of coil packages per cell | 1 | 1 | 3 |
| Number of coils in the coil package | 2 | 2 | 2 |
| Length of each SC coil (mm) | 360.0 | 360.0 | 360.0 |
| Inner cryostat radius (mm) | 310.0 | 300.0 | 400.0 |
| SC coil inner radius (mm) | 334.0 | 324.0 | 429.0 |
| SC coil thickness (mm) | 9.6 | 9.6 | 9.6 |
| Support structure thickness (mm) | 6.4 | 6.4 | 6.4 |
| Magnet cryostat thickness at ends (mm) | 55.0 | 55.0 | 80.0 |
| Magnet cryostat thickness at center (mm) | 80.0 | 80.0 | 80.0 |
| Cold mass per magnet cell (kg) | 207.6 | 201.1 | 911.1 |
| Overall mass per magnet cell (kg) | 277.3 | 268.0 | 1151.1 |
| Magnet Electrical Parameters | | | |
| Average central induction (T) | 1.25 | 1.25 | 1.25 |
| On axis induction variation (%) | ± 2.5 | ± 2.5 | ± 2.2 |
| Peak induction in the windings (T) | ~ 1.6 | ~ 1.6 | ~ 1.6 |
| Number of turns per cell | 2532 | 2532 | 7596 |
| Magnet design current (A) | 392.8 | 392.8 | 392.8 |
| Magnet design operating temperature (K) | 4.4 | 4.4 | 4.4 |
| Conductor critical current at operating T (A) | ~ 1600 | ~ 1600 | ~ 1600 |
| Magnet stored energy per cell E (kJ) | 224 | 211 | 1103 |
| Magnet self inductance per cell (H) | 2.90 | 2.74 | 14.3 |
| Superconductor matrix J (A mm ⁻²) | 249 | 249 | 249 |
| EJ ² limit per magnet cell (J A ² m ⁻⁴) | 1.39×10^{22} | 1.31×10^{22} | 6.86×10^{22} |
| Quench protection method | quench-back | quench-back | quench-back |

4.6. Summary

Table 4.2: Power dissipation in the μ^+ collection mode.

| | Power (kW) | | | | |
|-----------|---------------|-------|-------|-----|------|
| | e | μ | π | K | p |
| positives | 0.42 | 2.02 | 0.14 | 0 | 0.86 |
| negatives | 0.43 | 1.29 | 0.24 | 0 | - |

Table 4.3: Power dissipation in the μ^- collection mode.

| | Power (kW) | | | | |
|-----------|---------------|-------|-------|-----|------|
| | e | μ | π | K | p |
| positives | 0.42 | 1.45 | 0.19 | 0 | 0.94 |
| negatives | 0.45 | 1.90 | 0.14 | 0 | - |

Table 4.4: Absorber parameters.

| Absorber | Length (cm) | Radius (cm) | Number | P (kW) | P_{tot} (kW) |
|-----------------|----------------|----------------|--------|---------------|-------------------|
| Minicool | 175 | 30 | 2 | ≈ 5 | ≈ 10 |
| SFOFO lattice 1 | 35 | 18 | 16 | ≈ 0.3 | ≈ 4 |
| SFOFO lattice 2 | 21 | 11 | 36 | ≈ 0.1 | ≈ 3 |

Bibliography

- [1] M.J. Burns, et al., *DARHT Accelerators Update and Plans for Initial Operation*, Proc. 1999 Acc. Conf., p.617.
- [2] P.C. VanderArend, et al., *15-Foot Bubble Chamber Safety Report*, National Accelerator Laboratory Report NAL-48-A-2624, July 1972, Vol. 3.
- [3] R. W. Carr *et al.*, *E158 Liquid Hydrogen Target Milestone Report*, April 21, 1999, <http://www.slac.stanford.edu/exp/e158/documents/target.ps.gz>.
- [4] *ASME Boiler and Pressure Vessel Code*, ANSI/ASME BPV-VIII-1 (American Society of Mechanical Engineers, New York, 1980), part UG-32.